

Transmission of Light Through Small Elliptical Apertures (Part 2)

Masud Mansuripur, Armis R. Zakharian and Jerome V. Moloney

Last month, in Part 1 of this column, we analyzed the interaction of light with a subwavelength elliptical aperture in a thin metal film. The incident plane wave was assumed to be linearly polarized along the ellipse's major axis. We showed, through numerical simulations based on the Finite Difference Time Domain (FDTD) method, that only a small fraction of the incident optical energy could pass through the aperture. In this second and final installment, we take up the case of incident polarization aligned with the ellipse's minor axis. This 90° rotation of the plane of polarization turns out to have a drastic effect on the transmission efficiency of the aperture. (The numbering of figures and references is contiguous with Part 1.)

Elliptical aperture illuminated with plane-wave polarized along the short axis

When the incident E -field is parallel to the minor axis of an elliptical aperture, the surface currents I_s deposit charges at and around the long side-walls of the aperture, as shown in Fig. 13. These oscillating charges radiate as an electric dipole flanked by a pair of magnetic dipoles, creating circulating magnetic fields around the ellipse's minor axis that push the incident B -lines upward and sideways. In the area surrounding the hole, the E -field produced by these dipoles bends the I_s lines toward the mid-section of the aperture as shown in Fig. 13, and as required for self-consistency.

Aside from the incident beam, all the radiation in the system of Fig. 13 is produced by the surface currents I_s and the charges created by these currents. Subtracting the (uniform) surface current in the system of Fig. 2 from that in Fig. 13 thus yields the current distribution of Fig. 14(a), which is responsible for the difference between the radiation patterns in the two systems. When added to the uniform current of Fig. 2, the currents of Fig. 14(a) produce the I_s pattern shown in Fig. 13. The current loops of Fig. 14(a) are equivalent to a pair of oppositely oriented magnetic dipoles, $+m$ and $-m$, while the charges deposited on the long sides of the aperture constitute an electric dipole p ; see Fig. 14(b). Figure 14(c) shows that, in the XY -plane immediately above the aperture, the E -field is dominated by the electric dipole p . The contribution of the magnetic dipoles is to enhance the E -field at the center of the aperture, while weakening it in the outer regions.

Figure 14(d) shows that in the XY -plane directly above the aperture, the B -field profile is shaped by competition between the electric dipole p and the magnetic dipoles $\pm m$. The electric dipole dominates near the center but, further away, the magnetic dipoles dictate the B -field's behavior. The dotted B -lines near the sharp corners of the ellipse in Fig. 14(d) show the field leaving the XY -plane to enter/exit the hole.

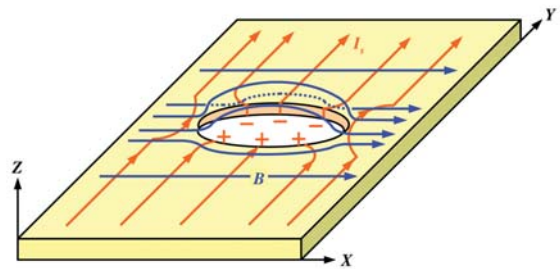


Figure 13. When the incident E -field is parallel to the minor axis of an elliptical aperture, the surface currents I_s deposit charges at and around the long side-walls of the aperture. These oscillating charges radiate as an electric dipole flanked by a pair of magnetic dipoles, creating circulating magnetic fields around the ellipse's minor axis that push the incident B -lines upward and sideways.

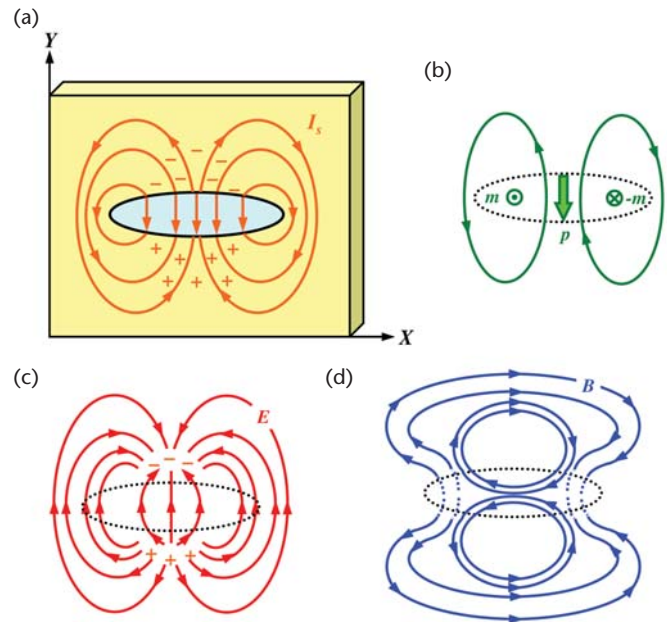


Figure 14. (a) Surface currents and the accompanying charge distribution produced by the elliptical aperture of Fig. 13. When added to the uniform current of Fig. 2, these currents produce the I_s pattern shown in Fig. 13. (b) The current loops in (a) are equivalent to a pair of magnetic dipoles, $\pm m$, while the charges deposited on opposite sides of the aperture constitute an electric dipole p . (c) In the XY -plane immediately above the aperture, the E -field is dominated by the electric dipole p . (d) In the XY -plane immediately above the aperture, the B -field profile is shaped by competition between the electric dipole p and the magnetic dipoles $\pm m$. Dotted B -lines near the sharp corners of the ellipse show the B -field leaving the XY -plane to enter/exit the hole.

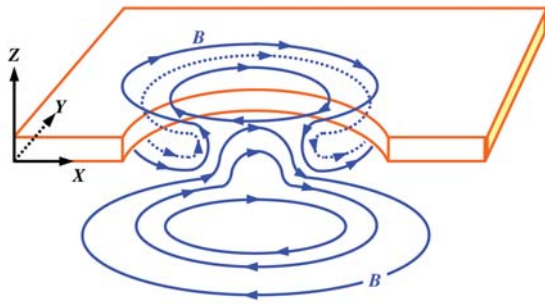


Figure 15. With reference to Fig. 14(b), the B -field of the electric dipole p combines with that of the magnetic dipoles $\pm m$ to produce closed loops in and around the aperture. The solid B -lines bulge above and below the metal film, while the dashed B -lines hug the conductor's top and bottom surfaces.

leaving the XY -plane to enter/exit the hole vertically (i.e., in the Z -direction). Although not shown in this figure, B -lines that enter the hole from above, close the loop by circling beneath the metal film and returning through the hole to reconnect with the B -lines above the film; see Fig. 15.

The surface charges and currents of Fig. 14(a) create magnetic fields in the free-space regions inside the hole as well as those above and below the metal surface. The B -field of the electric dipole p combines with that of the magnetic dipoles $\pm m$ to produce closed loops in the vicinity of the aperture, as shown in Fig. 15. The solid B -lines in this figure bulge above and below the metal surface, while the dashed lines hug the conductor's top and bottom surfaces. (The B -field cannot penetrate into the conductor, but, as it emerges from the hole, it bends above and below the surface in such a way as to bring the field lines close to the metallic surface.) In all cases, the lines of B must form closed loops to guarantee the divergence-free nature of the field. Since neither E - nor B -fields can exist within the conductor, the fields radiated by the electric dipole p must cancel out those of the magnetic dipoles $\pm m$ everywhere inside the metallic medium. The radiation emanating from these dipoles, however, permeates the interior of the hole as well as the free-space regions on both sides of the conductor. To get in and out of the hole, the B -lines of Fig. 15 appear to descend through one of the current loops that constitutes a magnetic dipole in Fig. 14(b), then return through the other loop. Note the change of direction of the magnetic field at the upper surface of the elliptical aperture: the direction of B just above the hole is opposite to that beneath the hole's upper surface. This 180° phase shift, dictated by the presence of the (uniform) I_s on the top surface of the elliptical aperture in Fig. 14(a), will disappear when the fringes of Fig. 2 are added to the fields produced by p , m and $-m$ to yield the total field in and around the aperture.

The induced electric charges on the surfaces surrounding the aperture produce an oscillating E -field in the short gap between the long side-walls as well as in the regions immediately above and below the aperture. The time rate of change of this field,

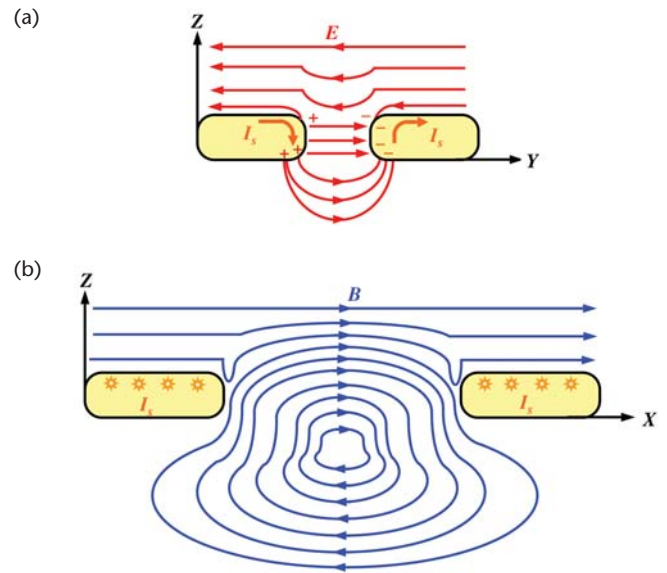


Figure 16. Cross-sections of the system of Fig. 13 in YZ - and XZ -planes. (a) The charges accumulating on the aperture's side-walls produce an E -field opposite in direction to the incident field. The lines of E may now start on positive charges and end on negative charges. (b) The dipoles p , m , and $-m$ of Fig. 14(b) push the B -fringe above the aperture upward and sideways to make room for circulating B -fields that surround the short axis of the elliptical aperture.

$\partial D/\partial t$, which is equivalent to an electric current density J across the gap, creates circulating magnetic fields around the short axis of the ellipse.⁴ These B -fields by themselves, however, are not sufficient to explain the field profile depicted in Fig. 15, and must be augmented by the fields produced by the circulating currents around the ellipse's sharp corners (i.e., the $\pm m$ dipoles) to yield a complete picture. Moreover, inside the metallic medium, the E - and B -fields of the p dipole cannot vanish without the compensating contributions of the $\pm m$ dipoles.

Figure 16 shows cross-sections of the system of Fig. 13 in YZ - and XZ -planes. Since I_s lags 90° behind the incident E -field immediately above the aperture, the accumulating charges on and around the side-walls produce electric fields opposite in direction to the incident E -field. The E -lines may now start on positive charges and end on negative charges ($\nabla \cdot D = \rho$), as shown in Fig. 16(a). This change of direction of the E -field causes a 180° phase shift in E_y from above to below the aperture. The E -fringe just above the aperture thus becomes weaker, sharing some of its energy with the E -field inside and below the aperture.

The XZ cross-section of the system of Fig. 13 depicted in Fig. 16(b) shows how the oscillating electric dipole p and magnetic dipoles $\pm m$ push the B -fringe above the aperture upward and sideways to make room for circulating B -fields that surround the short axis of the elliptical aperture. The resulting redistribution of the magnetic energy of the B -fringe above the hole thus makes it possible for some of the energy stored in this

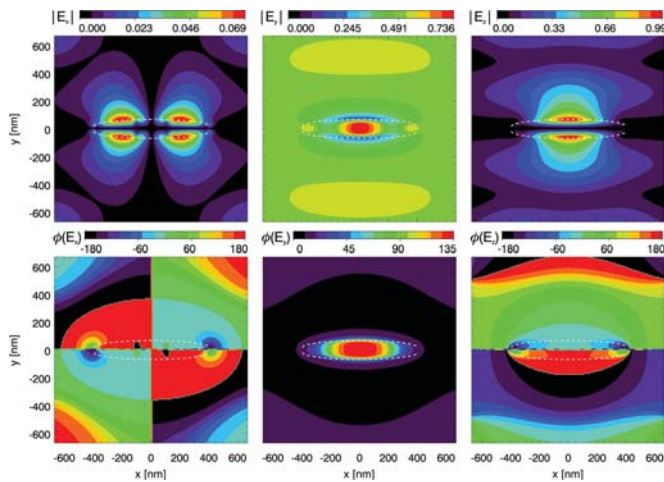


Figure 17. Computed plots of E_x , E_y , E_z in the XY-plane 20 nm above the conductor's surface in the system of Fig. 13. Top row: amplitude, bottom row: phase. The silver film is 124 nm-thick, the aperture is 800 nm-long and 100 nm-wide, and the radiation wavelength is $\lambda = 1 \mu\text{m}$. The aperture boundaries are indicated with dashed lines.

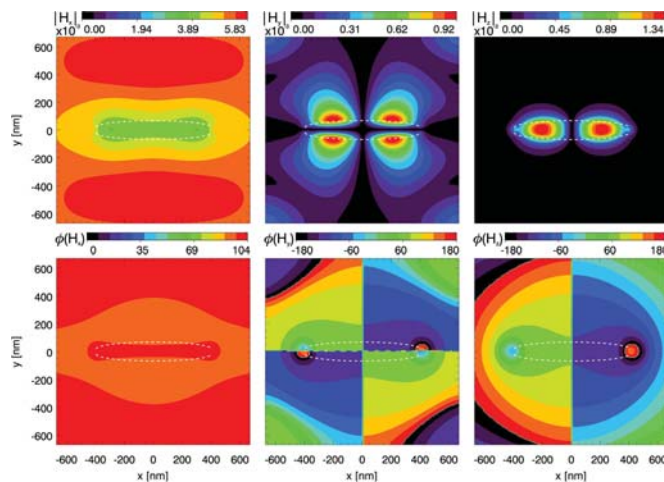


Figure 19. Computed plots of H_x , H_y , H_z in the XY-plane 20 nm above the surface of the conductor in the system of Fig. 13. Top row: amplitude, bottom row: phase. The aperture boundaries are indicated with dashed lines.

fringe to leak into the hole as well as the space below the hole. (The B -field distribution inside the aperture and in the region below the metal film is the same as that in Fig. 15, since the added fringes contribute only to the half-space above the conductor.) The divergence-free nature of the B -lines requires their continuity, which is evident in Fig. 16(b), in contrast to the E -lines of Fig. 16(a), which break up whenever they meet electrical charges.

Figure 17 shows computed plots of E_x , E_y , E_z in the XY-plane 20 nm above the surface of the conductor in the system of Fig. 13 (top row: magnitude, bottom row: phase). As before,

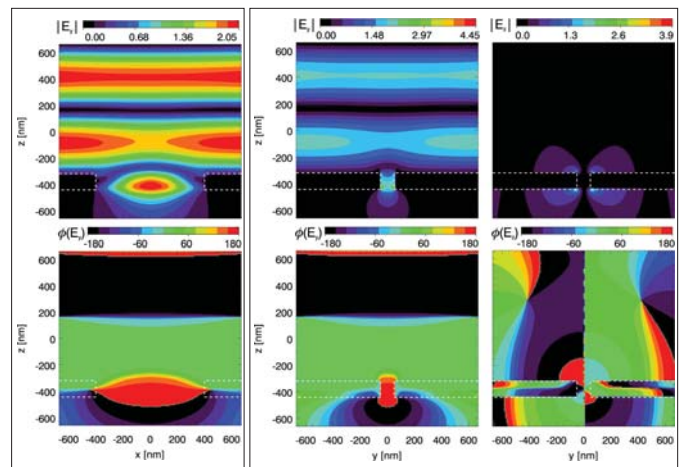


Figure 18. (Left) amplitude and phase of E_y in the central XZ-plane; (right) amplitude and phase of E_y , E_z in the central YZ-plane in the system of Fig. 13. The silver film's cross-section is indicated with dashed lines. The fringes in the two panels are differently colored because the color scale for E_y in the YZ-plane has been greatly expanded by two (barely visible) hot spots on the sidewalls near the bottom of the hole.

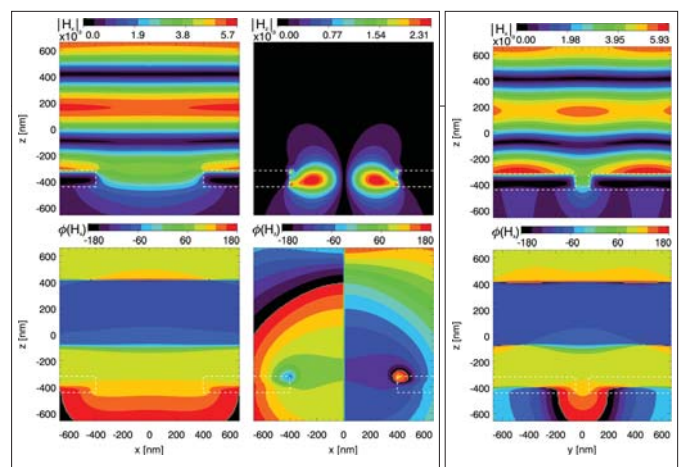


Figure 20. (Left) amplitude and phase of H_x , H_z in the central XZ-plane; (right) amplitude and phase of H_x in the central YZ-plane in the system of Fig. 13. The silver film's cross-section is indicated with dashed lines.

the 124 nm-thick silver film used in these simulations has $n + ik = 0.226 + i6.99$ at $\lambda = 1.0 \mu\text{m}$, and the ellipse's diameters along its major and minor axes are 800 nm and 100 nm, respectively.⁷ The strong z -component of E indicates the presence of significant amounts of electric charge on the conducting surfaces in the vicinity of the hole; the sign-reversal of E_z from one side of the hole to the other shows that the charges on the two sides have opposite signs.

Figure 18, left panel, shows the amplitude and phase of E_y in the central XZ-plane, while the right panel shows E_y , E_z in the central YZ-plane. Inside and below the aperture E_y is seen to be

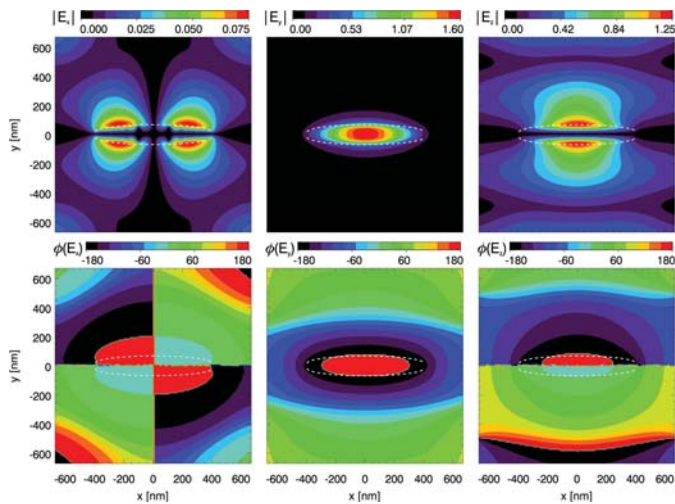


Figure 21. Computed plots of E_x , E_y , E_z in the XY-plane 20 nm below the bottom facet of the conductor in the system of Fig. 13. Top row: amplitude, bottom row: phase.

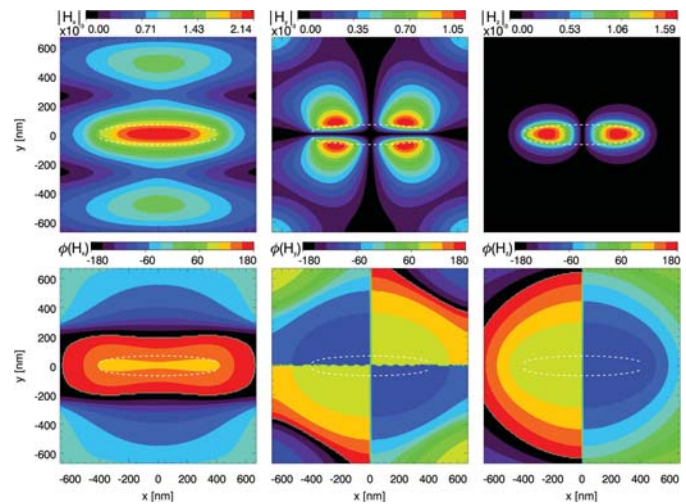


Figure 22. Computed plots of H_x , H_y , H_z in the XY-plane 20 nm below the bottom facet of the conductor in the system of Fig. 13. Top row: amplitude, bottom row: phase.

strong, and to have reversed direction relative to the E -field immediately above the aperture; its energy appears to have been extracted from the E -fringe directly above the hole. The distribution of E_z shows, once again, the presence of electric charges on the top and bottom surfaces of the conductor; these charges have the same sign on the top and bottom surfaces on either side of the hole, but their sign is reversed in going from the left-side to the right-side.

Computed plots of H_x , H_y , H_z in the XY-plane 20 nm above the conductor's surface appear in Fig. 19. Figure 20, left panel, depicts the amplitude and phase of H_x , H_z in the central XZ cross-section, while the right panel shows the distribution of H_x in the central YZ-plane. The magnetic field's behavior in these pictures is in accord with the qualitative behavior sketched in Fig. 16(b). Note, in particular, that the profile of H_z in Fig. 20 resembles the z -component of the circulating B -field in Fig. 16(b). Note also the draining of magnetic energy out of the B -fringe above the hole, and its redistribution not only in the form of magnetic fields inside and below the aperture, but also in the enhanced values of H_x directly above the conductor's surface.

Plots of E_x , E_y , E_z in the XY-plane 20 nm below the bottom surface of the conductor are shown in Fig. 21, and the corresponding magnetic-field plots appear in Fig. 22. These pictures are in full agreement with the qualitative diagrams of Figs. 14-16.

Figure 23 shows distributions of the magnitude $|S|$ of the Poynting vector in various cross-sections of the system of Fig. 13. The superimposed arrows on each plot show the projection of S in the corresponding plane.⁷ For instance, in the XZ cross-section depicted in (a) the arrows represent $S_x x + S_z z$, whereas in the YZ cross-section of (b) the arrows correspond to

the projection of the Poynting vector on the YZ-plane, namely, $S_y y + S_z z$. The plots in Figs. 23(c) and (d) show the distributions of $|S|$ in the XY-planes 20 nm above and below the aperture. In the absence of an aperture, S is essentially zero everywhere, as the reflected beam cancels out the incident beam's energy flux. When the aperture is present, however, the fields are redistributed in such a way as to draw the incident optical energy toward the aperture. The energy flows in from the region directly above as well as from the periphery of the hole in every direction. In addition to the straight-ahead energy, some of the peripheral energy also goes through the hole, thus enhancing the overall transmission. Further away from the aperture, especially in the YZ-plane (which contains the ellipse's short axis), the peripheral incoming energy turns away from the aperture and returns to the source.

The magnitude of the Poynting vector in the center at the bottom of the hole is $|S| \sim 1.23 \times 10^{-3} \text{ W/m}^2$, which is consistent with the transmitted E - and B -fields of $\sim 1.6 \text{ V/m}$ and $\sim 2.14 \times 10^{-3} \text{ A/m}$, with a phase difference $\Delta\phi = \phi_E - \phi_B \sim 45^\circ$ (see Figs. 21 and 22). The transmission efficiency of the optical power density at the center of this aperture is thus $\eta \sim 93\%$, which is nearly 500 times greater than that obtained when the incident polarization was parallel to the ellipse's long axis. (η is the ratio of $|S|$ at the aperture's center just below the conductor to the incident plane-wave's optical power density, $|S_{\text{inc}}| \sim 1.32 \times 10^{-3} \text{ W/m}^2$.) Several factors appear to have contributed to this strong performance (compared to the case of parallel polarization), among them, more electrical charges and stronger surface currents (especially on the bottom facet of the conductor), and a greater separation between the $\pm m$ magnetic dipoles, which tend to cancel each other out when they are close together.

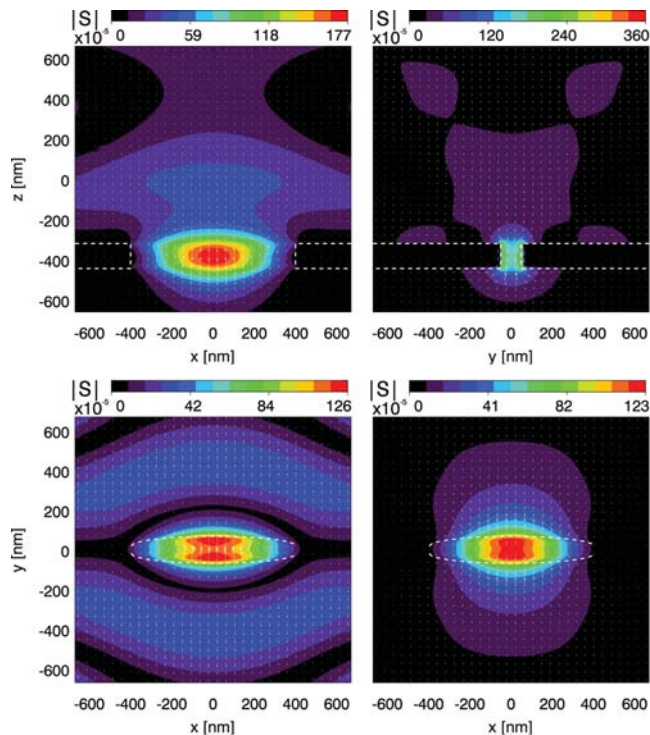


Figure 23. Profiles of the magnitude $|S|$ of the Poynting vector in various cross-sections of the system of Fig. 13. The superimposed arrows show the projection of S in the corresponding plane. (a) Central XZ-plane. (b) Central YZ plane. (c, d) XY-planes located 20 nm above and below the aperture.

Concluding remarks

We have analyzed the transmission of light through small elliptical apertures in a thin silver film at $\lambda = 1.0 \mu\text{m}$. Both cases of incident polarization parallel and perpendicular to the major axis of the ellipse were considered. The transmission efficiency η was found to be low for parallel polarization and high for perpendicular polarization.

The hallmark of the low-transmission case was a weak excitation of electric and magnetic dipoles on the upper surface of the metal film, which produced even weaker excitations on the lower surface. Although not described here, we have observed similar behavior for a circular aperture (diameter = 100nm, silver film thickness = 124nm, $\eta = 0.06\%$ at the center of the aperture 20nm below the conductor), and also for an infinitely long, 100nm-wide slit ($\eta = 0.14\%$ at the center of the slit 36nm below the bottom facet; incident polarization parallel to the slit). For the elliptical hole under low-transmission conditions, η drops rapidly with an increasing film thickness h , from 0.2% at $h = 124\text{nm}$, to 0.008% at $h = 186\text{nm}$, and to below 0.001% at $h = 248\text{nm}$. It appears that the elliptical hole, when considered as a waveguide,^{8,9} does not support any guided mode whose E -field is predominantly aligned with the ellipse's long axis.

The high-transmission ellipse revealed the excitation of fairly strong electric and magnetic dipoles on the upper surface of the metal film, which induced even stronger dipoles on the film's lower facet. In this case η remains high for thicker films as well ($\eta = 93\%$ for $h = 124\text{nm}$, 86% for $h = 186\text{nm}$, and 136% for $h = 248\text{nm}$), indicating propagation through the hole (along the Z-axis) of a guided mode whose E -field is largely parallel to the ellipse's short axis. We also found that an infinitely long, 100nm-wide slit exhibits strong transmission for an incident polarization aligned with the narrow dimension of the slit ($\eta \sim 69\%$ at the center of the slit, 36nm below a 124nm-thick silver film).

It thus appears that achieving a large η requires an aperture that can excite strong oscillator(s) on the upper surface of the film, which would then induce strong oscillations on the lower facet, thereby creating the conditions for the passage of a substantial amount of electro-magnetic energy through the sub-wavelength opening in the metal film. The ability of a hole (or slit) to support a guided mode that can be excited by the incident polarization appears to be critical for achieving large transmission, especially for thicker films. Recent reports of various aperture designs that have significant throughputs (compared with simple circular or square-shaped apertures)^{3,10} indicate that the aforementioned principles, far from being specific to elliptical holes in thin metal films, have a broad range of application.

Acknowledgments

The authors are grateful to Dennis Howe, Pavel Polynkin, Ewan M. Wright, and Pierre Meystre of the Optical Sciences Center for many helpful discussions.

OPN contributing editor Masud Mansuripur (masud@u.arizona.edu) is a professor of optical sciences at the University of Arizona in Tucson. His collection of past OPN columns has been published in *Classical Optics and Its Applications* (Cambridge University Press, UK, 2002). Armis Zakharian and Jerome Moloney are with the Department of Mathematics and the Optical Sciences Center at the University of Arizona. This work has been supported by AFOSR contract F49620-03-1-0194.

References

1. M. Born and E. Wolf, *Principles of Optics*, 7th edition, Cambridge University Press, UK (1999).
2. H. A. Bethe, "Theory of diffraction by small holes," *Phys. Rev.* **66**, 163 (1944).
3. T. Thio, K. M. Pellerin, R. A. Linke, H. J. Lezec, and T. W. Ebbesen, "Enhanced light transmission through a single subwavelength aperture," *Opt. Lett.* **26**, 1972-4 (2001).
4. J. D. Jackson, *Classical Electrodynamics*, 2nd edition, Wiley, New York, 1975.
5. A. Taflov and S. C. Hagness, *Computational Electrodynamics*, Artech House (2000).
6. Jin Au Kong, *Electromagnetic Wave Theory*, EMW Publishing, Cambridge, Massachusetts, 2000.
7. The computer simulations reported in this article were performed by Sim3D_Max™, a product of MM Research, Inc., Tucson, Arizona.
8. J. A. Porto, F. J. Garcia-Vidal, and J. B. Pendry, "Transmission resonances on metallic gratings with very narrow slits," *Phys. Rev. Lett.* **83** (14), 2845-8 (1999).
9. Q. Cao and P. Lalanne, "Negative role of surface plasmons in the transmission of metallic gratings with very narrow slits," *Phys. Rev. Lett.* **88** (5), 57403 (2002).
10. X. Shi, L. Hesselink, and R. L. Thornton, "Ultrahigh light transmission through a C-shaped nanoaperture," *Opt. Lett.* **28** (15), 1320-2 (2003).